

A Real-Time Detection Pipeline for Transient Sources in Radio Images using Convolutional Neural Networks

David Ruhe^{2,1,*}, Mark Kuiack¹, Antonia Rowlinson¹, Ralph Wijers¹, Patrick Forré²

Abstract

In recent years, survey facilities have started to provide remarkable new opportunities for transient astronomy. This is made possible by combining unprecedented fields of view with high sensitivity in uninvestigated wavelength regimes. The result of this combination is an extremely high volume of data to be analysed. In this work, we have opened up the way to real-time automated analysis of the image data-stream. We present a fully automated GPU-based machine-learning backed pipeline for analysis of radio images at multiple frequencies. It consists of four consecutive steps: quality control, source detection, association, flux measurement and physical parameter inference. At the end of the pipeline, an alert of a significant detection can be sent out and data will be saved for further investigation.

In our current implementation, the entire pipeline analyses images from AARTFAAC (Amsterdam Astron Radio Transients Facility And Analysis Centre) with sizes upwards of $16 \times 1024 \times 1024$ pixels. AARTFAAC is a transient detector based on the Low-Frequency Array, an interferometer based in the Netherlands with stations across Europe. First results show that dispersed signals were found on which follow-up analysis can be performed. The identification and response to transients is the key science goal for AARTFAAC, and the current work brings us one step closer to meeting it.

Keywords:

radio transients, image processing, streaming data analysis, machine learning, neural networks

1. Introduction

In antiquity, transient astronomical events that were visible to the naked eye were extremely rare, and recordings of observations are sometimes hundreds of years apart. Due to its very narrow field of view, the classical telescope did not improve chances of observing such transient events; the odds of looking in exactly the right place at the right time are simply too small. With the advent of instruments that have large (even all-sky) fields of view in relatively unexplored frequency domains the search for these transients has gained significant interest (Staley et al., 2013; Booth and Jonas, 2012; Murphy et al., 2013; Tingay et al., 2013; Taylor et al., 2012; van Haarlem et al., 2013; Rowlinson et al., 2016; Ivezić et al., 2019; Kuiack et al., 2020a). The radio regime now also has entered this area of time-domain all-sky astronomy with transients being one of the key objectives (Taylor et al., 2012; Murphy et al., 2013; Tingay et al., 2013; van Haarlem et al., 2013; Bell et al., 2011; Pintaldi et al., 2021).

Transient hunting is among LOFAR's key science objectives (Fender et al., 2006), as it is for the future radio telescope SKA (Carilli and Rawlings, 2004). Of interest are sources that vary on sub-second timescales to multi-year variability. Among the LOFAR transient programs, there is the Amsterdam ASTRON

Radio Transients Facility and Analysis Centre (AARTFAAC) (Prasad et al., 2016). AARTFAAC is a sensitive all-sky (centered on Zenith) transients program with a spatial resolution of 10s of arcmin at low frequencies (30 – 80 MHz). It was developed to utilize either 6 (AARTFAAC6) or 12 (AARTFAAC12) of LOFAR's core stations and expand the transient discovery space to wider fields with shorter time-resolutions (down to 1 second). The key advantage is a real-time imaging pipeline that can be analysed in a streaming fashion. Its foremost goal is blindly to search for the brightest and rarest transients, filtering only the most useful information, and alerting the multi-wavelength transient community when required. It is infeasible to archive all data that are generated by AARTFAAC. Therefore, only data containing potentially interesting candidates should be stored. This requires that the enormous number of spurious candidates, from radio frequency interference (RFI), scintillating sources, and random noise, that comes with the data stream have to be filtered automatically.

Swinbank et al. (2015) paved the way towards detecting astronomical transients by automatically obtaining, analyzing and storing light-curves of the sources from multi-epoch observations using the LOFAR Transients Pipeline (TraP). The authors focused on the accuracy of associations between epochs and the precision of measurements in their methodology, aiming to improve computation speeds toward streaming analysis in future work. Unfortunately, no such real-time pipeline has been realised yet. Inspired by Swinbank et al. (2015), this work pinpoints the essential components of such a pipeline while pre-

*Corresponding author at: Anton Pannekoek Institute, University of Amsterdam, Amsterdam, 1098XH, The Netherlands

Email address: d.ruhe@uva.nl (David Ruhe)

¹Anton Pannekoek Institute, University of Amsterdam

²AI4Science (AMLab), Informatics Institute, University of Amsterdam

serving accuracy. We resort to using AARTFAAC as a dedicated transient detector (i.e., to generate alerts for the community), as opposed to a more involved analysis pipeline. [Kuiack et al. \(2020a\)](#) have developed methods for analysis of light-curves while reducing detections of spurious sources: e.g. (correlated) noise, interference, satellites and airplanes), on which some of the methods in the current work were based. Summarizing, our contributions are as follows:

- A source detection strategy based on convolutions.
- A neural-network based analysis approach, in which physical parameters are inferred from dynamic spectrum plots.
- An end-to-end GPU-accelerated pipeline that can take streaming image data and output alerts in real-time. It consists of source detection, tracking (i.e., association) and analysis³.

The paper is organised as follows. In [section 2](#) we discuss the instrument (AARTFAAC) and data products that the current methodology was designed for as well as some of the simulations that were used in this study. We like to stress that while this pipeline was developed for AARTFAAC (specifically AARTFAAC6), no instrument-specific parameters have been set and it is expected to work on a range of instruments (e.g., [Prasad et al. \(2016\)](#); [Anderson et al. \(2019\)](#); [Pintaldi et al. \(2021\)](#)). Notably, we expect to continue its application and development on AARTFAAC12. Throughout, we report performance on simulated data reminiscent of AARTFAAC12 and even higher dimensionalities. In [section 3](#) we describe the end-to-end pipeline and its methodologies. In [section 4](#) we report results of experiments that were done to test the pipeline and some preliminary data products extracted from application to observations. Finally, we conclude in [section 5](#) and foresee some interesting directions for further research and development.

2. Instrument, Observations & Simulations

2.1. Instrument & Observations

Though intended to be generally applicable, the methods presented in this paper were designed using AARTFAAC. AARTFAAC is a wide-field, fast cadence imaging, low-frequency radio facility designed to survey the Northern Hemisphere for bright low-frequency (30 – 80 MHz) transient events. It specialises in transients that evolve on timescales from one second to several minutes. It can process data coming from LOFAR’s low-band antennae (LBA) simultaneously with other LOFAR observations. AARTFAAC uses 288 (576) dipoles and 6 (12) central LOFAR stations, resulting in a maximum baseline of 300m (1.5 km). It obtains a spatial resolution of 1° (20 arcmin) at 60MHz. Sensitivity is best at Zenith, decreasing while approaching the horizon due to radio frequency interference and lower antenna sensitivity. Correlation, calibration and imaging can already be done in

streaming mode for AARTFAAC-6 ([Prasad et al., 2016](#)). The brightest sources in the sky: Cygnus A, Cassiopeia A, Taurus A, Virgo A and the Sun are removed prior to imaging (in visibility space). Finally, primary beam correction is applied, flattening the antenna response across the field of view ([Kuiack et al., 2019](#)).

For development of the methods in this study sixteen observing bands arranged in two sets of 8 consecutive subbands of 195.3 kHz calibrated bandwidth each, leading to two bands at 57.6MHz through 59.0 MHz and 61.1 MHz through 62.5 MHz, were used. The integration time is 1 second. Examples of AARTFAAC-6 images are given in [A.10](#).

2.2. Transient Simulation

For our inference procedure (see [Section 3.4](#)) the most informative data product is the frequency-time intensity data, or dynamic spectrum, which is the final product of our data pipeline. Using this array, we want to estimate (as fast as possible) physical parameters which help to classify the type of signal detected. As specified earlier, to infer these parameters we will employ a neural network. Since we have few true transient candidates, we are very short on data to train a neural network. Favorably, we know one of the most important properties of a true astrophysical transient: a bright, broadband, dispersed signal. The dispersion of the signal is manifested through the broadening of the pulse over a finite bandwidth. It originates from interaction of the emitted photons with electrons along the path between an observer and the source. Thus, assuming a uniform density of free electrons, it gives an indication of the distance that a signal has traveled. The integrated electron column density, called the dispersion measure (DM), is used as a proxy for the distance to the source. Using known equations, we can easily simulate dispersed astrophysical transients. The DM of non-astrophysical transients usually is close to 0 (i.e., no broadening of the pulse), making the DM possibly the most useful feature for separating signal from noise ([Kuiack et al., 2020b](#)). We build a dataset by injecting these simulated pulses into randomly sampled noise from the survey. In the following, the reported values parameters and can be set according to the interests of the practitioner. They should be set such that the simulated dataset covers the population of interest sufficiently. First, we generate a Gaussian pulse profile using a width sampled uniformly between 0 and 16, corresponding to a maximum FWHM of 37.67 seconds. The profile is computed as

$$f(t, w) = \exp\left[-\left(\frac{t}{w}\right)^2\right] \quad (1)$$

centered around t_0 . For each frequency ν of the survey, we compute the arrival time by applying a dispersion delay

$$t_\nu = t_0 + C_{\text{DM}} \text{DM} (\nu^{-2} - \nu_0^{-2}) \quad (2)$$

with C_{DM} the dispersion constant $\frac{e^2 \text{pc}}{8\pi^2 \epsilon_0 m_e c} \cdot 10^{-6} \approx 4148.806 \text{ MHz}^2 \text{cm}^{-3} \text{ms}$ ([Lorimer and Kramer, 2012](#)). In this analysis, we sample the DM uniformly between 0 and 512, covering a

³Code is publicly available at <https://ascl.net/2103.015> ([Ruhe et al., 2021](#))

significant part of the known FRB population (Petroff et al., 2016). The final intensity is computed as

$$I(\nu, t) = A \left(\frac{\nu}{\nu_0} \right)^\alpha f(t - t_\nu, \nu) \quad (3)$$

where A is the burst amplitude (arbitrary units), assuming a standard normal noise level. We experimented with A uniformly between 0 and 32 and α , the spectral index, sampled from $(-4, 4)$ uniformly. We compute the intensity for all time-steps and frequencies and save the pulse at the corresponding band and time indices. Using this procedure, we create 32,768 samples (input time-frequency plots and output parameters pairs) to train the network. Let $\epsilon \in M \times T$ be a spatially integrated AARTFAAC-6 noise sample of T consecutive time-steps at a random spatial location at M frequencies. We sample 16,384 of such, using a maximum of 256 sample locations per individual sequence. This gives us $2^{14} \cdot 2^{16} = 2^{30} = 1,073,741,824$ possible signal-noise combinations. This number increases even more when one considers all the temporal indices t_0 that the transient signal can be centered around in the data-point. In this paper, we run experiments with $T = 64$ and we centered the inserted transients around $t_0 \sim U(0, 64)$. This enhances (next to the chosen network architecture, see Section 3.4) temporal invariance of the neural network. Examples are given in Figure 1. It is clear from the examples that AARTFAAC6 operates with two separated consecutive ranges of sub-bands⁴.

2.3. Skymap Simulation

To test the source-finder, we carry out experiments using simulated all-sky images. This has the advantage that we control entirely the noise characteristics and SNR of the sources. First, we generate a model that simulates large-scale inhomogeneities of the final image. E.g., our Galactic foreground noise and Cygnus A & Cassiopeia A calibration remnants. An example is given in Appendix B. Then, we add to this map standard, independent Gaussian noise. Finally, we add point sources at log-normally sampled flux densities $s \sim \log \mathcal{N}(\mu, \sigma^2)$, resulting in a flux distribution that has most of the density centered at a certain SNR, but with significant outliers. These outliers cause substantial side-lobes throughout the image, testing our source-finder's robustness. Finally, we convolve this image with a circularly symmetric low-pass filter, whose impulse response is given by

$$h[n_1, n_2] = \frac{\omega_c}{2\pi \sqrt{n_1^2 + n_2^2}} J_1(\omega_c \sqrt{n_1^2 + n_2^2}) \quad (4)$$

where J_1 is the Bessel function of the first kind and order and we have $h[0, 0] = \frac{\omega_c^2}{4\pi}$. ω_c is a parameter that controls the size of the beam. Single-channel and integrated examples are given in Appendix B.

⁴We tested which configuration (e.g., two separate ranges, one continuous range) of sub-bands resulted in the best parameter estimates (subsection 3.4) and actually found that a single range works better.

3. Methodology

Here we sub-divide the entire pipeline into four distinct sections. Where needed, we first give required preliminary terminology or knowledge. An overview of the pipeline is given in Figure 2.

3.1. Quality Control

As specified earlier, we consider all 16 images output by the imaging pipeline. This is motivated triply. First, the dispersed signal of astrophysical (extra-galactical) transients means that integrating them over frequency with incorrect adjustment for dispersion will wash out the signal. For this reason, we perform source detection and analysis in all subbands simultaneously (for more details, see subsection 3.2). Second, occasionally one of these can be highly corrupted after strong interference, causing the correlation & imaging pipeline to shoot to extreme values. Integrating these directly would cause the entire time-step to be lost, as this corrupted sub-band will dominate the statistics. Third, we can use the availability of images at multiple subbands to detect and filter terrestrial and near-Earth RFI which appears undispersed. We describe these last two cases in the following.

Take an image-cube $\mathbf{X}_t \in \mathbb{R}^{C \times D \times D}$ at time-step t consisting of C images of size $D \times D$, each corresponding to an individual sub-band. For AARTFAAC6, we have $C = 16$ and $D = 1024$. If available, \mathbf{X}_t is loaded into GPU memory. If any of these individual sub-band images is extremely corrupted, we simply filter it out based on maximum absolute value: $\max \text{abs}(\mathbf{x}_i) > e$, where \mathbf{x}_i is a single sub-band in \mathbf{X}_t . Images that exceed the threshold are imputed with zeroes. An example of such poor quality image is given in Figure A.12.

Now, we deal with the RFI cases. Though less obvious than the previously dealt with corruptions, strong RFI needs to be filtered as the side-lobes throughout the image will cause many false positives downstream. These occur rather frequently, but favorably have a narrow bandwidth and often occur in only one bandpass. The filtering is done based on a mean-square distance threshold and normalizing using robust statistics. The idea is that we can leverage the fact that we have images coming from C central frequencies at the same time, assuming that the majority of these are uncorrupted. We compute the median image by taking the pixel-wise median over the N images. We square the difference of each image with this median and calculate the image mean for all of these. This gives us a list \mathbf{s} of C distance scores. Next, we calculate the median and median absolute deviation of this list and standardize the scores.

$$\mathbf{z} = \frac{\mathbf{s} - \text{median}(\mathbf{s})}{\text{MAD}(\mathbf{s})} \quad (5)$$

where MAD stands for Median Absolute Deviation (e.g. Howell, 2005). Since we use robust center and spread statistics, outliers are easily picked up on. Using $z_h = 5$ we found empirically that this is a very accurate approach to filtering RFI-corrupted images.

On simulated data, we tested by modelling RFI as extremely bright single-band point sources (1 to 4 times the PSNR). We

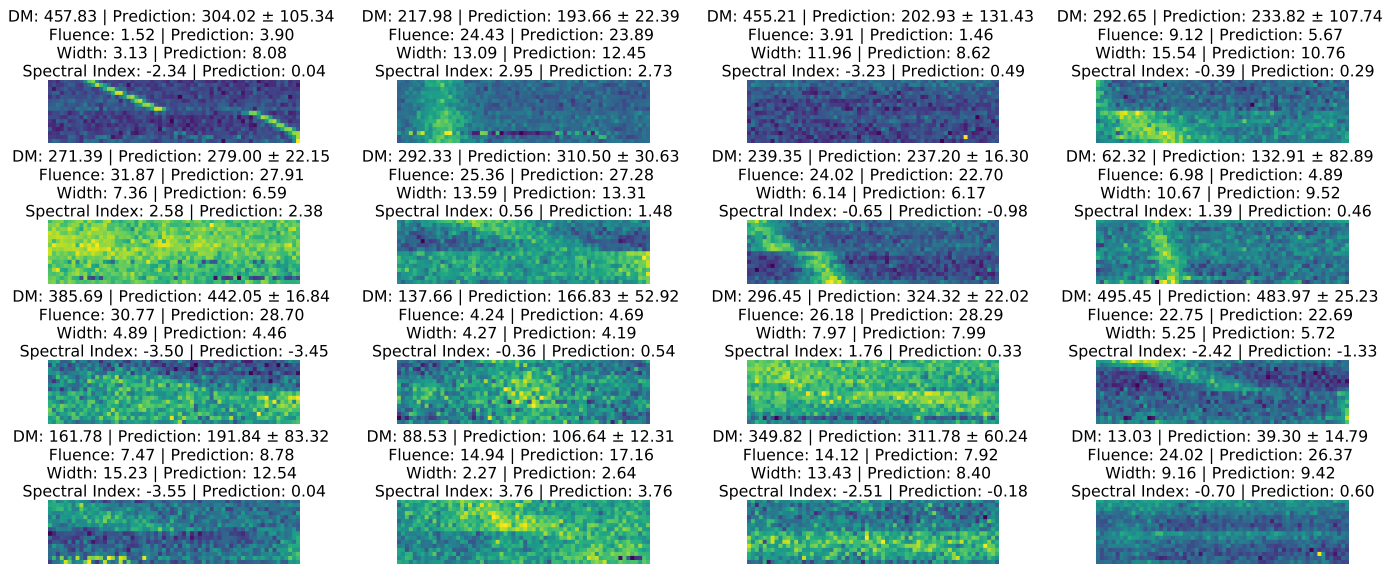


Figure 1: Examples of generated pulses injected into AARTFAAC6 noise. We denote the parameters that the pulse was simulated with, as well as the predictions that the neural network output.

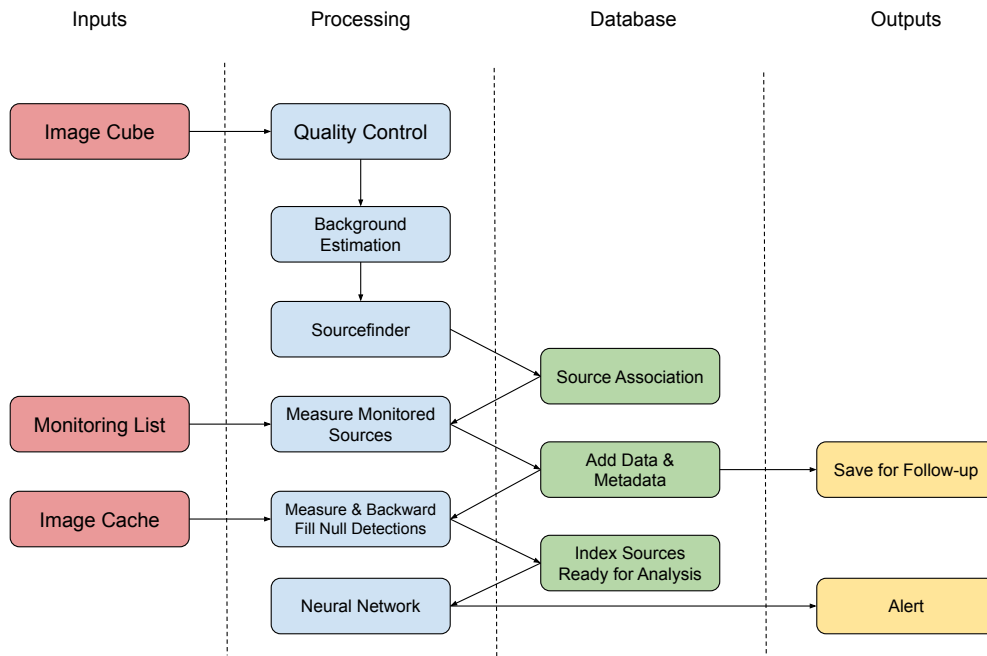


Figure 2: Overview of all the steps in the proposed pipeline.

retrieved 87% of the RFI corrupted images. Note that this is relatively mild RFI, so the false negatives are no surprise. Also, as the concern might arise that a highly dispersed transient might only appear in one channel, risking it to be filtered out as RFI⁵. However, reassuringly we report zero false positives for these.

Images that exceed this threshold are imputed with zeroes. Note that this is a standardized score, thus not sensitive to user-specified settings or the particular survey. Examples of RFI detections that were one subband adjacent to the clean images presented in Figure A.10 are given in Figure A.11.

3.2. Source Detection

We analyse images at multiple bandpasses at the same time in parallel and optionally on GPUs. This is done since astronomical transients are expected to be dispersed over these bandpasses, and integrating them out before searching would decrease their SNRs. This case is e.g. applied in Anderson et al. (2019). Additionally, by searching in sub-bands separately we obtain a type 2 error improvement without many assumptions. This in contrast to applying coherent dedispersion before searching, which is practically unattainable to achieve for all possible DM on all-sky images in real time. We show this statistically in Appendix E.

3.2.1. Peak Detection

Swinbank et al. (2015) and Spreeuw et al. (2018) divide the image to be analysed into a grid. In every patch, sigma-clipping is performed and thus local statistics are used for the detection threshold. We substitute this approach with a method that combines sigma-clipping with convolutions. This is doubly motivated. First, when dividing the image into a grid, an isolated faint source might not be detected when it is at the edge of a grid patch that is crowded with bright sources (or RFI). The bright objects have to be clipped away for the source to be found. Another rather naive way to overcome this is to use interpolation of the statistics. Alternatively, one might want to sigma-clip using overlapping patches, lowering the risk that a faint source at an unfortunate position might not be picked up on. However, this simply becomes a convolution if taken to the extreme case where we use patch statistics at every pixel coordinate. Second, by the convolution theorem, this can effectively be implemented using Fourier transforms and accelerated on GPUs.

Let

$$G(n, m) = \frac{1}{Z} \exp \left[-\frac{1}{2\sigma^2} (n^2 + m^2) \right] \quad (6)$$

be a Gaussian kernel with normalising constant (i.e., it sums to unity) $Z = \sum_{n=-k}^k \sum_{m=-k}^k \exp \left[-\frac{1}{2\sigma^2} (n^2 + m^2) \right]$. Alternatively, one could also go for a (circular) uniform kernel. σ is a parameter, and should be set such that the local background statistics are sufficiently included, without incorporating too much source flux. Heuristics for setting it are e.g. widening the Gaussian such that its FWHM includes most primary side-lobes, or running an optimization scheme such that it retrieves as many as possible

⁵The robustness of the pipeline is displayed here: <https://youtu.be/grZX9dVxXzk>. Note the stability of the detected sources.

known sources from a reference catalog. Then at each iteration we have

$$C_c = G * X_c \quad (7)$$

and

$$S_c = G * (X_c - C_c)^2 \quad (8)$$

where the square is applied element-wise. C_{cmm} and S_{cmm} are center and spread estimates computed at every location. We clip values in the following manner:

$$y_{cij} = \mathbb{I}(x_{cij} > c_{cij} + \kappa \sqrt{s_{cij}}) \quad (9)$$

with κ as a parameter that specifies how much signal is required for a detection to be made. This procedure is repeated until no new y_{cij} is discovered. The result of the iterative local sigma-clipping is a map $\mathbf{Y} \in \{0, 1\}^{C \times D \times D}$ indicating the source locations.

3.2.2. Peak Localization

In order to obtain the peak locations and values, we apply a maximum filter to \mathbf{X} and compute a map $\mathbf{Z} \in \{0, 1\}^{C \times D \times D}$ indicating if the pixels are the local maximum:

$$z_{c,i,j} = \mathbb{I}(x_{c,i,j} = \max\{x_{c,n,m} \mid n, m \in \{i-k, \dots, i+k\} \times \{j-k, \dots, j+k\}\}) \quad (10)$$

with $k = 3$. Then, we obtain the peak locations $\mathbf{P} \in \{0, 1\}^{C \times D \times D}$ by the following boolean operation:

$$p_{cij} = z_{cij} \wedge y_{cij}. \quad (11)$$

Intuitively, we only include pixels that are both the local maximum and above the detection threshold, giving us the exact location of the peaks. The advantage of doing so (next to parallelization) is that this automatically deblends detected sources. I.e., it separates an ‘‘island’’ of flux that exceeds the local noise level into two distinct sources.

This concludes the source detection & localization pipeline. The advantages of all the previous operations are two-fold. First, they are fully parallel and accelerated on GPUs. That is, all operations are performed concurrently on separate spatial locations of the arrays. The performance of these are further discussed in section 4. Second, they are agnostic to survey specifics and only use standardised approaches and values, which should generalise well to other data.

3.3. Source Association & Flux Measurement

Our association methodology is a rather simplified version compared to the sophisticated techniques of Swinbank et al. (2015). This is done to be able to run the entire pipeline in real-time. Note that the following (except for the flux measurement) is not GPU-accelerated anymore. GPU-accelerated source association is left for a future iteration of the pipeline. At time-step t , after we obtain a list of sources from the source detection pipeline we filter the duplicates that we obtain from measuring at different frequencies simultaneously.

Next, we match to the catalog’s previous time-step $t - 1$ sources based on the 2D distance (in degrees). Sources are

matched if they are within a pre-specified association distance limit (e.g., 1 degrees for AARTFAAC-6). Next to one-to-one, the matches can be of the kind one-to-many or many-to-one (Swinbank et al., 2015), but in the interest of compute time we do not consider these as the typical surface density of sources on the sky does not give rise to these edge cases often. Rather, they are left as new detections, thereby matching only the closest source.

We concatenate the detected sources table with the sources that are to be monitored. When a detection is done, we keep taking measurements until it has not been detected for at least a pre-specified number of time-steps. This is to obtain data-products that are not too sparse for analysis.

Next, we take measurements of the fluxes of the detected sources at all frequencies. This is done by taking the maximum pixel value within a box around the source peak. Again, in the interest of time, we are not fitting and integrating Gaussians to the detected sources. We add the measured peak flux to the database for every monitored or newly detected source.

We backward fill the catalogue with newly detected sources. That is, if some potential transient is detected in time-step t , we also want to include the “build-up” into the data-products. Thus, we add a pre-specified number of timesteps to the catalogue and measure from cached images.

Finally, we add the current time-step’s images to the cache.

3.4. Neural Network-based Parameter Inference

Our source detection pipeline already filters out spurious candidates based on local noise statistics. However, in radio astronomy there exist many noise modes (e.g., RFI, satellites, airplanes) that will slip through as candidate transients. Kuiack et al. (2020a) have performed significant steps for filtering out these. In this work we need a highly parallelizable filter. For this reason, we resort to machine learning. Neural networks in particular can process many data instances in parallel, especially on GPUs (LeCun et al., 2015). In this subsection we elaborate how we use inferred physical parameters to filter the spurious transient candidates. Afterwards, we give an introduction to deep learning and convolutional neural networks (LeCun et al., 1995). Finally, we explain how we these are used to obtain physical parameters.

3.4.1. Filtering Candidates Based On Physical Parameters

An astrophysical pulse or burst can be described using a range of physical parameters. For radio transients these are, among others, overall shape, integrated and peak flux density, pulse width, dispersion measure, spectral information (such as index and bandwidth), and scattering. By obtaining these, we can quickly apply a filter and narrow follow-up investigation to only the most interesting cases. For example, any noise progenitor that is relatively close (e.g., atmospheric or human-made) will not be dispersed since the integrated electron density along the path is too small. If we can quickly obtain the dispersion measure (corrected with a SNR estimate) we can exclude low-DM bursts. Next, we give an introduction to deep learning and how it is used to infer these parameters of interest.

3.4.2. Deep Learning

We briefly discuss the set-up of the neural network, but for a more thorough explanation of how the neural network can be used on frequency-time plots we refer the reader to e.g. (Connor and van Leeuwen, 2018). In its essence, a neural network is a regression preceded with a series of nonlinear transformations. The idea is that the network learns a mapping from input space to another space (“hidden state”) from which it completes a task (e.g., classification or regression). The projection into the hidden space allows a neural network to learn a representation. This representation reflects important features that were computed from the input data. A hidden state is computed using a linear combination of the input with a set of weights, and a nonlinearity (referred to as “activation function”) $\phi(\cdot)$:

$$z = \phi(\mathbf{x}^T \mathbf{w} + b). \quad (12)$$

In this work we use Leaky ReLU functions:

$$\phi(z) = \begin{cases} z & \text{for } z \geq 0 \\ \alpha z & \text{for } z < 0 \end{cases} \quad (13)$$

with α a small positive value. Concatenating multiple of such layers with a final task-specific layer forms a neural network. Since we are dealing with a regression problem here (inferring parameters from the dynamic spectra) our final layer is simply another linear combination, but without an activation function.

Convolutional neural networks (LeCun et al., 1995) are a type of neural network where the weight vector comes in the form of a filter (or kernel) and the input image is convolved with this filter. This weight filter is then learned, extracting relevant features from the image (e.g., edges). This can, like a traditional feed-forward network, be optimized with regular gradient descent and backpropagation (LeCun et al., 2015). The fact that only kernels (typically multiple per layer) are learned, makes this a lightweight network that is particularly effective for image processing. Applying the kernels in a convolution also has the advantage that the network output is translationally invariant. We did not use pooling operators for dimensionality reduction, but simply applied our convolutions with “strides” of 2. An overview of the used architecture is given in Figure 3⁶.

3.4.3. Parameter Inference

The output of the neural network determines the distribution $p(\boldsymbol{\theta} | \mathbf{x})$ that the network is modelling. Here, $\boldsymbol{\theta}$ is the parameter of interest and \mathbf{x} is the data product. For example, if we take a logistic regression (which essentially is the final layer of a neural network without any preceding transformations): $\sigma(\mathbf{w}^T \mathbf{x} + b)$ where σ is the logistic sigmoid function, we can model a Bernoulli distribution since the output will always be a value in $(0, 1)$. Thus, we can use this to e.g. classify (the classical machine learning example) cats versus dogs. In this work, we model real-valued parameters. Therefore, our final layer does not incorporate a nonlinearity (such as the sigmoid), and the

⁶Generated using <http://alexlenail.me/NN-SVG/AlexNet.html>

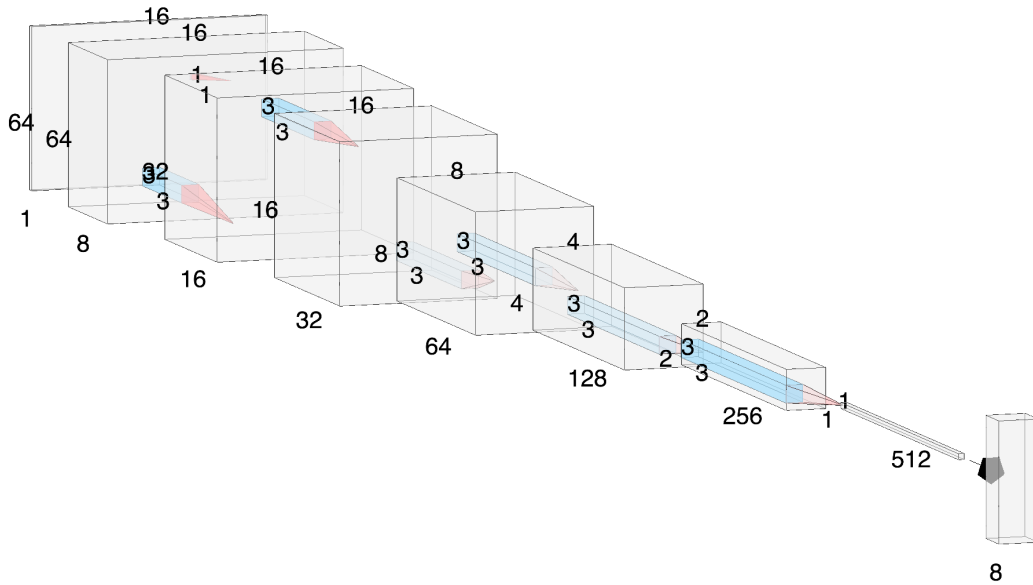


Figure 3: Illustration of the used neural network architecture in this paper. The input is a $1 \times 64 \times 16$ dynamic spectrum. By applying strided convolutions the width and height of the spectrum decreases, but the depth (so called “feature maps”) increases. At the end of the network we are left with a $512 \times 1 \times 1$ vector, which is passed through a linear layer to obtain 8 inferred parameters and standard deviations.

distribution we model is a Gaussian. Let

$$\begin{bmatrix} \hat{\mu} \\ \hat{\sigma} \end{bmatrix} = \mathbf{g}(\mathbf{x}, \mathbf{W}) \quad (14)$$

be the output of the neural network $\mathbf{g}(\mathbf{x}, \mathbf{W})$, where \mathbf{W} is the concatenation of the layer weights. Under this model, the likelihood of the “target” parameters θ and the network’s prediction is given by $\mathcal{N}_{\mathbf{W}}(\theta | \hat{\mu}, \text{diag}(\hat{\sigma}))$. Using batch gradient descent, we iteratively maximize this likelihood function, obtaining the set of weights

$$\mathbf{W}^* := \arg \max_{\mathbf{W}} \mathcal{N}_{\mathbf{W}}(\theta | \hat{\mu}, \text{diag}(\hat{\sigma})) \quad (15)$$

that maximizes it.

By outputting a predicted variance, the network directly models the SNR in a data-point. This allows for filtering data-points with too low SNR levels. More on this in [section 4](#).

4. Results

In this section we discuss the tests we applied to the pipeline, as well as the preliminary results that were observed after testing it on real observations.

4.1. Pipeline Testing

Here we lay out an overview of the experiments we ran to test the pipeline. The following are run on an Intel Xeon Gold 5118 with a maximum clock speed of 3.20 GHz and an NVIDIA Titan RTX GPU accelerator.

4.1.1. Performance & Scaling

In [Figure 4](#) we see that we can process images in a fraction of the time that [Swinbank et al. \(2015\)](#) will take. For this comparison, consider [Figure 5](#). Also comparably, [Pintaldi et al. \(2021\)](#) report 924 images processed in 13 hours. Favourably, we see that the processing time as a function of number of pixels scales sub-linearly. There is little overhead added by our convolutional source localization: the bulk of compute is required for catalog processing and image caching. Specifically, backward filling (see [subsection 3.3](#)) takes 37% of this sub-step, and image caching takes 60%, increasing with image size. Smart I/O can solve this, but will be left for future work. Finally, inferring directly parameters using a neural network adds little overhead.

4.1.2. Accuracy of Source Finding

Regarding accuracy of the source-finder, we conducted two experiments. In the first one, we simulate an entire source field. The procedure is given in [Section 2](#). The reported SNRs (x -axis) are computed by dividing the peak flux value over the local noise as estimated by PySE. We report results in precision, recall, and F1 scores. The F1 score computes a harmonic mean between precision (P) and recall (R).

$$P = \frac{TP}{TP + FP} \quad (16)$$

$$R = \frac{TP}{TP + FN} \quad (17)$$

$$F1 = \frac{2PR}{(P + R)} \quad (18)$$

where TP and FP are the number of true positives and false positives, respectively. In [Figure 6](#) we compare our results with

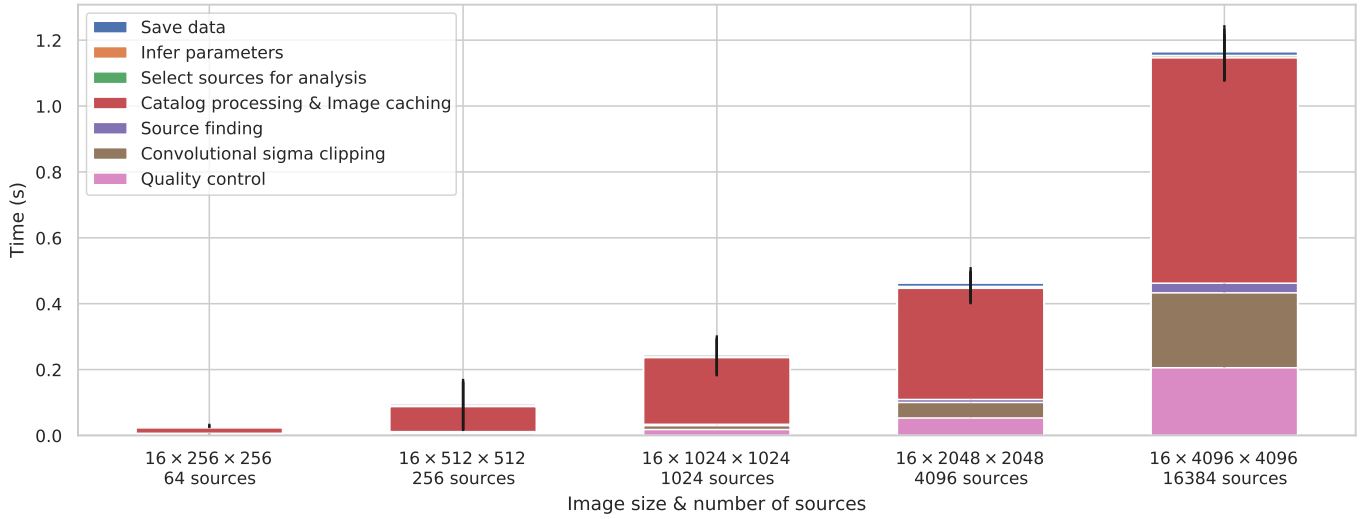


Figure 4: Scaling of the entire pipeline and the individual steps for different image sizes and source numbers.

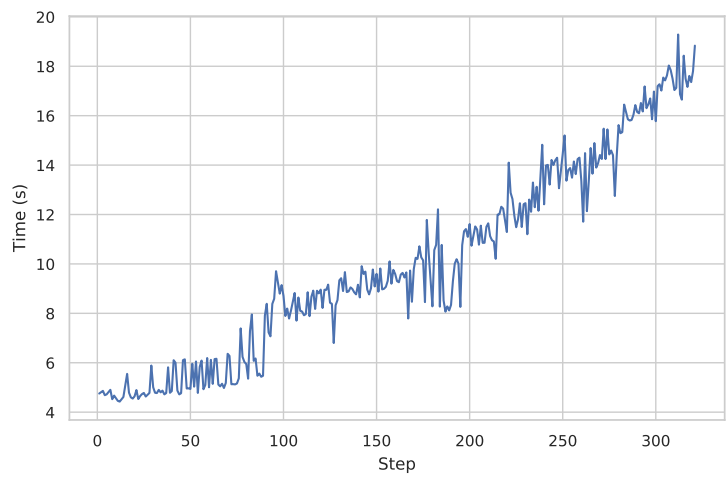
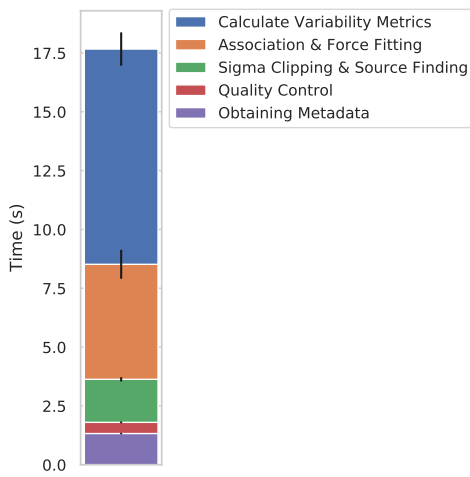


Figure 5: Left: Timing of the Swinbank et al. (2015) pipeline for 16 1024×1024 images. Right: due to the extensive association procedure and variability metrics calculation, the time taken per image scales superlinearly and thus is prohibitive for lengthy observations.

Fluence	0	5	10	15	20	25
MAE	27.45	18.31	13.39	11.62	10.32	9.48
RMSE	52.02	32.78	21.61	17.09	15.14	12.66
1σ	0.7010	0.7092	0.7089	0.7006	0.7079	0.6985
2σ	0.9655	0.9637	0.9615	0.9584	0.9607	0.9654
3σ	0.9962	0.9956	0.9955	0.9947	0.9959	0.9945

Table 1: Quantitative results of the neural network prediction of the DM parameter. The column labels are cutoff fluence values (i.e., at 5 we only consider bursts with fluences above 5). Experiment is performed under the simulation and neural network settings that are described in the current paper.

PySE (Spreeuw et al., 2018) at various SNR. We see that with increasing source SNR, the recall increases, as expected. We obtain high precision at low SNRs, since only few sources will pass the detection threshold. It drops with higher source signal, as there will be more spurious side-lobes and other artefacts that are picked up on. For high SNR sources the precision becomes a bit better, as many side-lobes will not be detected anymore. Both approaches are highly comparable.

Next, we insert sources into real observations. We use images of the AARTFAAC6 all-sky survey (Prasad et al., 2016). Source intensities are sampled from a log-normal distribution. Again, we report results in precision, recall and F1 scores in Figure 7.

Examples of the resulting skymaps (with simulated sources marked) are given in Figure B.16. The findings are similar to the previous experiment.

4.1.3. DM Inference

The CNN was trained using early stopping. That is, training was not canceled until the likelihood on the held-out validation data stopped increasing. Quantitative results on the DM inference (arguably, the most important feature for discriminating spurious from real bursts) are shown in 1. The reported MAE (mean absolute error) and RMSE (root mean squared error) are satisfactory considering the range of values that DM can take. Most importantly, the true value lies within the predicted uncertainty range almost exactly the number of times we would expect it to.

Additional insight into the training results are given in Figure 8. In the first plot we see that the predicted DM of the bursts correlates well with the DM it was sampled with. On the extremes ends of the sampled DMs, the model is naturally conservative. In the second plot we see that the uncertainty increases on average for higher DMs. In the third plot we see that the highest likelihoods occur at low DMs. Finally, we see that the uncertainty increases for low-fluence bursts. Examples of ground truth (target) and predicted DMs and uncertainties are given in Figure 1.

4.2. Application to Real Data

We applied the pipeline to a real AARTFAAC-6 survey dataset. We used $\kappa = 4.5$ to retrieve an acceptable number of

candidate sources from the source detection pipeline. “Acceptable” here expresses a trade-off between precision and recall. By lowering κ , many more spurious candidates will be retrieved. The neural network will filter these, but the disadvantages are two-fold: more processing has to be done and it might start force-fitting at locations where you want to remain sensitive to actual candidates. After pushing the associated time-frequency data through the network, we obtain a dataset of parameters θ for every transient candidate. These can be filtered based on the scientist’s needs. To obtain examples of interesting bursts presented in this study, we used the following. We threshold $\hat{\mu}_{DM}$, the inferred DM at 50. Next, we use a SNR-standardized score $z = \frac{\hat{\mu}_{DM}}{\hat{\sigma}_{DM}}$ which we threshold at 4.5 as our second filter. By applying the entire pipeline to a real-time live survey we retrieved interesting candidates for follow-up analysis fully automatically. Examples are shown in Figure 9. The above is exemplary, but gives an idea how a practitioner can filter the data based on inferred physical parameters. The transient proposed by Kuiack et al. (2020a) was recovered with an estimated DM of 74.49 ± 8.26 (Kuiack et al. (2020a) concluded a DM of 74 ± 5). Based on the blind detections we performed so far, it is clear that just searching for broad-band dispersed signals is not enough. Scintillation seems to produce a plurality of the signals we are looking for, and we should find new ways to sift the distribution of these candidates from truly interesting events. Among others, this includes checking if there was no significant activity in the neighbourhood prior to the signal and correcting for known sources using a reference catalog.

5. Conclusion

The intention of this work was to develop new methods that allow for real-time analysis of all-sky radio images to search for transient sources. In order to do so, we presented a fully automated GPU-based machine-learning backed pipeline. It consists of four consecutive steps: quality control, peak detection, association & flux measurement and inference. To do peak detection, we propose accelerated convolutional sigma-clipping, source-detection and localization. It does both more and less than previous approaches (e.g., Swinbank et al. (2015)): it directly infers physical parameters from the data, but is less careful with source association in the interest of time. Results show that the precision and recall of source detections using this procedure compares with previous methods, at a fraction of the processing speed. After association, we employ a convolutional neural network to infer physical parameters from the running catalog frequency-time datapoints. Training results show that the neural network can infer these up to high precision. In addition to the actual parameters, the network also outputs an associated standard-deviation expressing an indication of SNR of the data-point. Combining these, we can filter non-interesting false positives rather easily. The entire pipeline can analyse image cubes upwards of $16\,1024 \times 1024$ images in under 1 second per iteration, meaning that the goal of real-time analysis is met. After applying the pipeline to real observations, dispersed signals were found on which follow-up analysis can be performed. All in all, we have shown that in the current era of high-dimensional

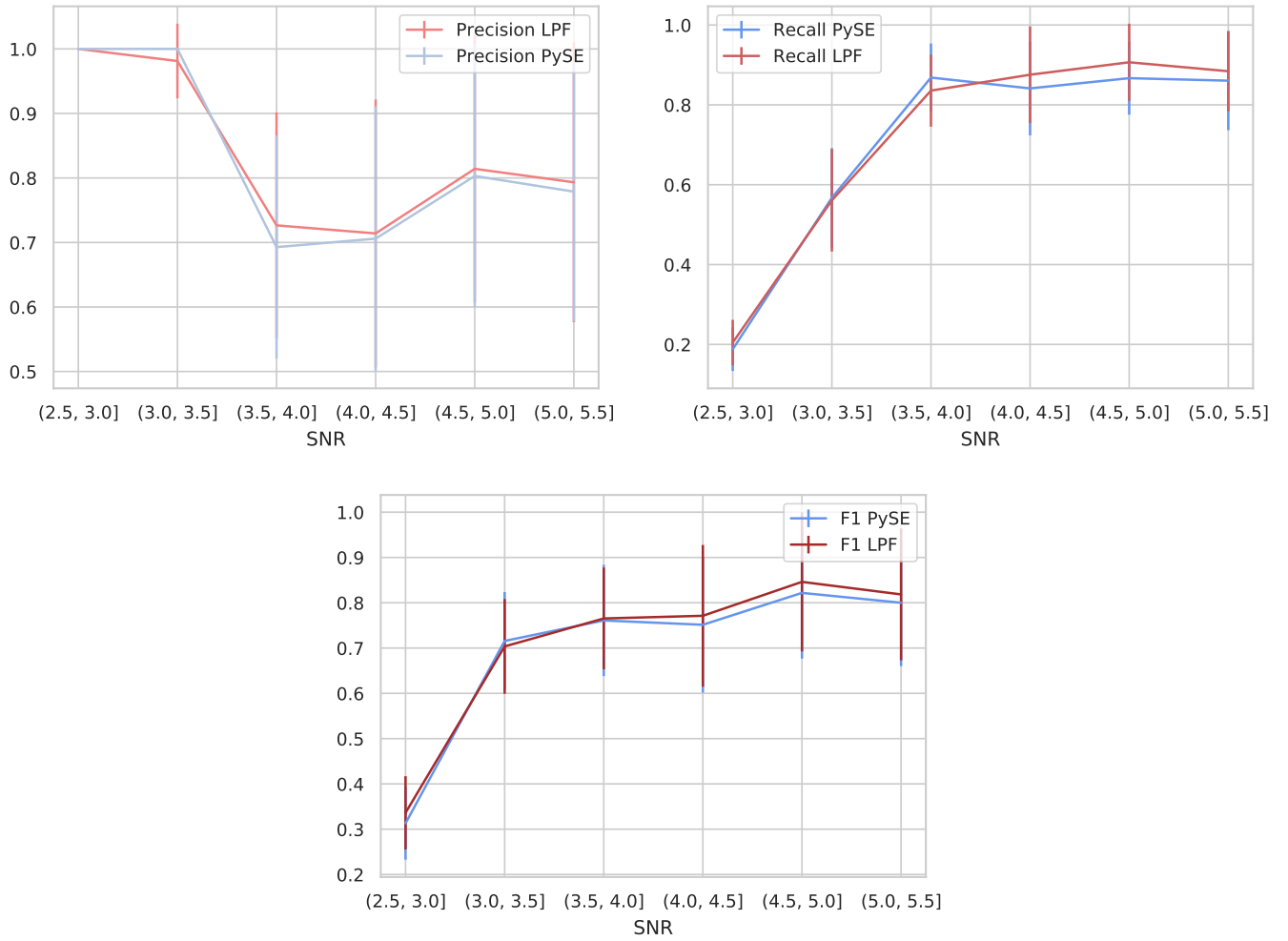


Figure 6: Precision, recall and F1 scores of the current work compared to PySE as baseline for simulated sky-maps.

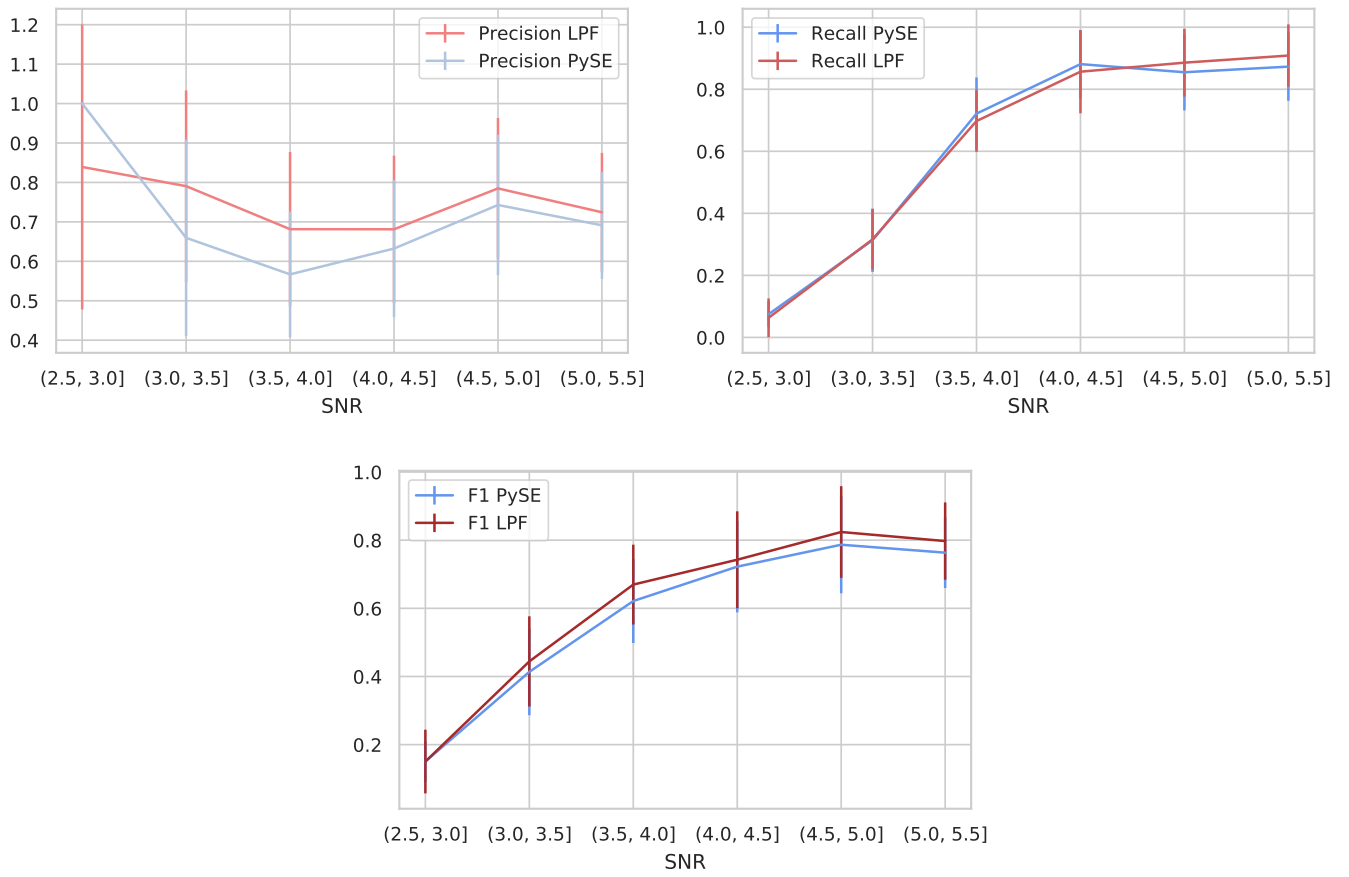


Figure 7: Precision, recall and F1 scores of the current work compared to PySE as baseline for AARTFAAC6 images with injected sources. Reported SNRs are single-subband.

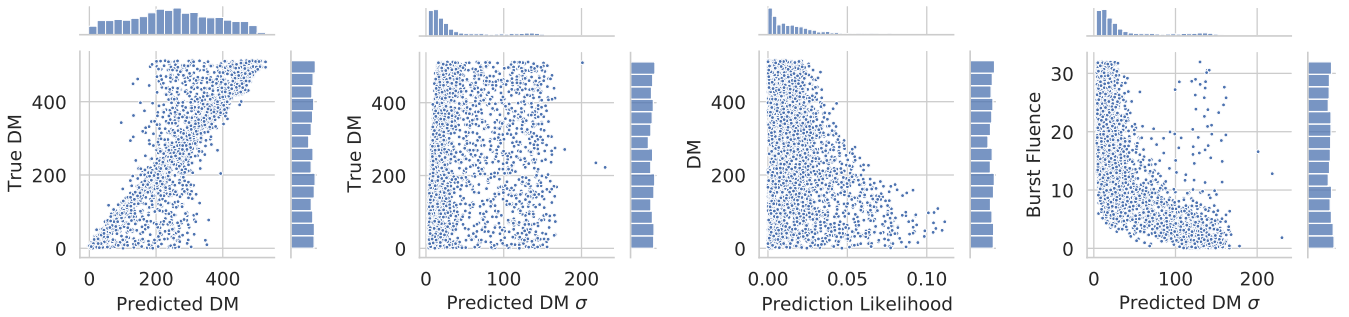


Figure 8: Neural network evaluation plots. From left to right: (1) how well the predicted DM corresponds to the true DM, (2) how the uncertainty changes for increasing DM, (3) how the likelihood changes for increasing DM and (4) how the uncertainty changes for increasing burst fluence.

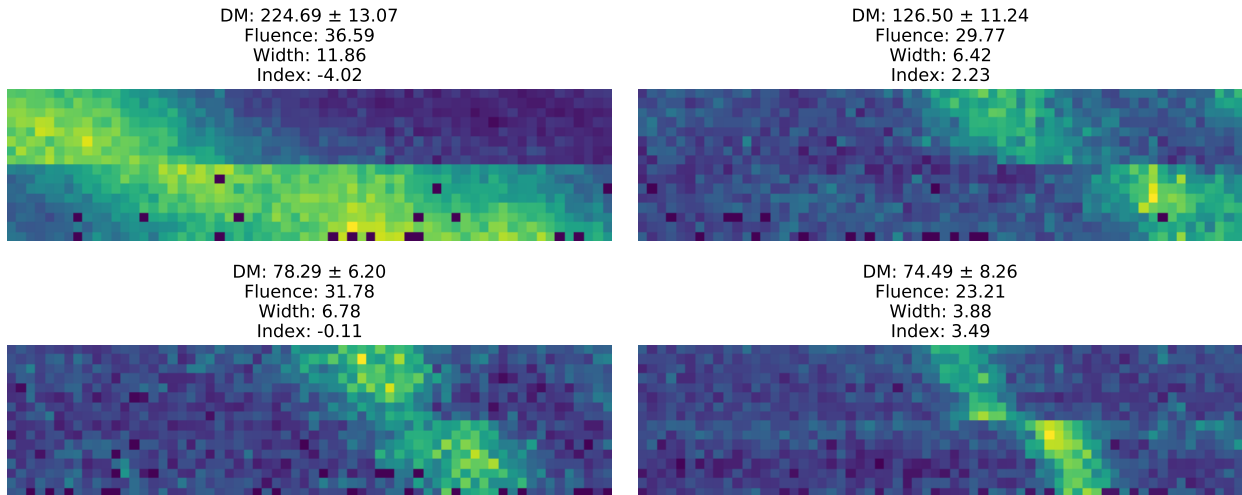


Figure 9: Examples of some real dispersed signals that were found after applying the pipeline. Specifically, the right-bottom example is the proposed candidate by Kuiack et al. (2020a).

all-sky astronomical streaming data, real-time analysis is feasible. This is a step forward for observatories like LOFAR’s AARTFAAC, having remarkably wide field-of-view and unique sensitivity to low radio frequencies.

6. Future Work

The current work greatly focused on removing the obstacles that disallowed real-time analysis. Now that these are out of the way, there is still room for improvement. Firstly, source association is not accelerated yet, and could be incorporated in a future version. Secondly, several dispersed signals were already found that seem spurious. Thus, separating these from true transients requires more than merely looking at dynamic spectra. Third, as large amounts of data can be processed using the proposed work, limits can be put on the transients surface density under AARTFAAC parameters. Finally, since the neural network seems to add very little overhead compared to the other steps, it might be feasible to just let it monitor every spatial coordinate in the image, skipping source-finding and association altogether.

7. Acknowledgements

This research made use of AstroPy (Price-Whelan et al., 2018), Pandas (McKinney et al., 2011), NumPy (Walt et al., 2011), SciPy (Virtanen et al., 2020), Matplotlib (Hunter, 2007) and PyTorch (Paszke et al., 2017). Accordingly, we would like to thank the scientific software development community, without whom this work would not be possible. This work was fully funded by the University of Amsterdam.

References

Anderson, M.M., Hallinan, G., Eastwood, M.W., Monroe, R.M., Callister, T.A., Dowell, J., Hicks, B., Huang, Y., Kassim, N.E., Kocz, J., et al., 2019. New limits on the low-frequency radio transient sky using 31 hr of all-sky data with the ovro-lwa. *The Astrophysical Journal* 886, 123.

Bell, M.E., Fender, R., Swinbank, J., Miller-Jones, J., Law, C., Scheers, B., Spreeuw, H., Wise, M., Stappers, B., Wijers, R., et al., 2011. An automated archival very large array transients survey. *Monthly Notices of the Royal Astronomical Society* 415, 2–10.

Booth, R., Jonas, J., 2012. An overview of the meerkat project. *African Skies* 16, 101.

Carilli, C., Rawlings, S., 2004. Science with the square kilometer array: Motivation, key science projects, standards and assumptions. *arXiv preprint astro-ph/0409274*.

Connor, L., van Leeuwen, J., 2018. Applying deep learning to fast radio burst classification. *The Astronomical Journal* 156, 256.

Fender, R., Braun, R., Stappers, B., Wijers, R., Wise, M., Coenen, T., Falcke, H., Griessmeier, J.M., Van Haarlem, M., Jonker, P., et al., 2006. The lofar transients key project. *arXiv preprint astro-ph/0611298*.

van Haarlem, M.P., Wise, M.W., Gunst, A., Heald, G., McKean, J.P., Hessels, J.W., de Bruyn, A.G., Nijboer, R., Swinbank, J., Fallows, R., et al., 2013. Lofar: The low-frequency array. *Astronomy & astrophysics* 556, A2.

Howell, D.C., 2005. Median absolute deviation. *Encyclopedia of statistics in behavioral science*.

Hunter, J.D., 2007. Matplotlib: A 2d graphics environment. *Computing in science & engineering* 9, 90–95.

Ivezić, Ž., Kahn, S.M., Tyson, J.A., Abel, B., Acosta, E., Allsman, R., Alonso, D., AlSayyad, Y., Anderson, S.F., Andrew, J., et al., 2019. Lsst: from science drivers to reference design and anticipated data products. *The Astrophysical Journal* 873, 111.

Kuiack, M., Huizinga, F., Molenaar, G., Prasad, P., Rowlinson, A., Wijers, R.A., 2019. Aartfaac flux density calibration and northern hemisphere catalogue at 60 mhz. *Monthly Notices of the Royal Astronomical Society* 482, 2502–2514.

Kuiack, M., Wijers, R.A., Shulevski, A., Rowlinson, A., Huizinga, F., Molenaar, G., Prasad, P., 2020a. The aartfaac 60 mhz transients survey. *arXiv preprint arXiv:2003.13289*.

Kuiack, M.J., Wijers, R.A., Shulevski, A., Rowlinson, A., 2020b. Apparent radio transients mapping the near-earth plasmaenvironment. *arXiv preprint arXiv:2003.11138*.

LeCun, Y., Bengio, Y., Hinton, G., 2015. Deep learning. *nature* 521, 436–444.

LeCun, Y., Bengio, Y., et al., 1995. Convolutional networks for images, speech, and time series. *The handbook of brain theory and neural networks* 3361, 1995.

Lorimer, D.R., Kramer, M., 2012. Handbook of pulsar astronomy. *Handbook of Pulsar Astronomy*.

McKinney, W., et al., 2011. pandas: a foundational python library for data analysis and statistics. *Python for High Performance and Scientific Computing* 14.

Murphy, T., Chatterjee, S., Kaplan, D.L., Banyer, J., Bell, M.E., Bignall, H.E., Bower, G.C., Cameron, R.A., Coward, D.M., Cordes, J.M., et al., 2013.

Vast: an askap survey for variables and slow transients. *Publications of the Astronomical Society of Australia* 30.

Paszke, A., Gross, S., Chintala, S., Chanan, G., Yang, E., DeVito, Z., Lin, Z., Desmaison, A., Antiga, L., Lerer, A., 2017. Automatic differentiation in pytorch .

Petroff, E., Barr, E., Jameson, A., Keane, E., Bailes, M., Kramer, M., Morello, V., Tabbara, D., Van Straten, W., 2016. Frbcat: the fast radio burst catalogue. arXiv preprint arXiv:1601.03547 .

Pintaldi, S., Stewart, A., O'Brien, A., Kaplan, D., Murphy, T., 2021. A scalable transient detection pipeline for the Australian SKA Pathfinder VAST survey. arXiv preprint arXiv:2101.05898 .

Prasad, P., Huizinga, F., Kooistra, E., van der Schuur, D., Gunst, A., Romein, J., Kuiack, M., Molenaar, G., Rowlinson, A., Swinbank, J.D., et al., 2016. The AARTFAAC all-sky monitor: System design and implementation. *Journal of Astronomical Instrumentation* 5, 1641008.

Price-Whelan, A.M., Sipőcz, B., Günther, H., Lim, P., Crawford, S., Conseil, S., Shupe, D., Craig, M., Dencheva, N., Ginsburg, A., et al., 2018. The Astropy project: Building an open-science project and status of the v2.0 core package. *The Astronomical Journal* 156, 123.

Rowlinson, A., Bell, M., Murphy, T., Trott, C., Hurley-Walker, N., Johnston, S., Tingay, S., Kaplan, D., Carbone, D., Hancock, P., et al., 2016. Limits on fast radio bursts and other transient sources at 182 MHz using the Murchison widefield array. *Monthly Notices of the Royal Astronomical Society* 458, 3506–3522.

Ruhe, D., Kuiack, M., Rowlinson, A., Wijers, R., Forré, P., 2021. LPF: Real-time detection of transient sources in radio data streams. [arXiv:2103.015](https://arxiv.org/abs/2103.015).

Spreeuw, H., Swinbank, J., Molenaar, G., Staley, T., Rol, E., Sanders, J., Scheers, B., Kuiack, M., 2018. Pyse: Python source extractor for radio astronomical images. *ascl*, ascl-1805.

Staley, T., Titterton, D., Fender, R., Swinbank, J., van der Horst, A., Rowlinson, A., Scaife, A., Grainge, K., Pooley, G., 2013. Automated rapid follow-up of Swift gamma-ray burst alerts at 15 GHz with the AMI large array. *Monthly Notices of the Royal Astronomical Society* 428, 3114–3120.

Swinbank, J.D., Staley, T.D., Molenaar, G.J., Rol, E., Rowlinson, A., Scheers, B., Spreeuw, H., Bell, M.E., Broderick, J.W., Carbone, D., et al., 2015. The LOFAR transients pipeline. *Astronomy and Computing* 11, 25–48.

Taylor, G., Ellingson, S., Kassim, N., Craig, J., Dowell, J., Wolfe, C., Hartman, J., Bernardi, G., Clarke, T., Cohen, A., et al., 2012. First light for the first station of the long wavelength array. *Journal of Astronomical Instrumentation* 1, 1250004.

Tingay, S.J., Goke, R., Bowman, J.D., Emrich, D., Ord, S.M., Mitchell, D.A., Morales, M.F., Boller, T., Crosse, B., Wayth, R.B., et al., 2013. The Murchison widefield array: The square kilometre array precursor at low radio frequencies. *Publications of the Astronomical Society of Australia* 30.

Virtanen, P., Gommers, R., Oliphant, T.E., Haberland, M., Reddy, T., Cournapeau, D., Burovski, E., Peterson, P., Weckesser, W., Bright, J., et al., 2020. Scipy 1.0: fundamental algorithms for scientific computing in Python. *Nature Methods* 17, 261–272.

Walt, S.v.d., Colbert, S.C., Varoquaux, G., 2011. The NumPy array: a structure for efficient numerical computation. *Computing in Science & Engineering* 13, 22–30.

Appendix A. AARTFAAC6 Image Examples

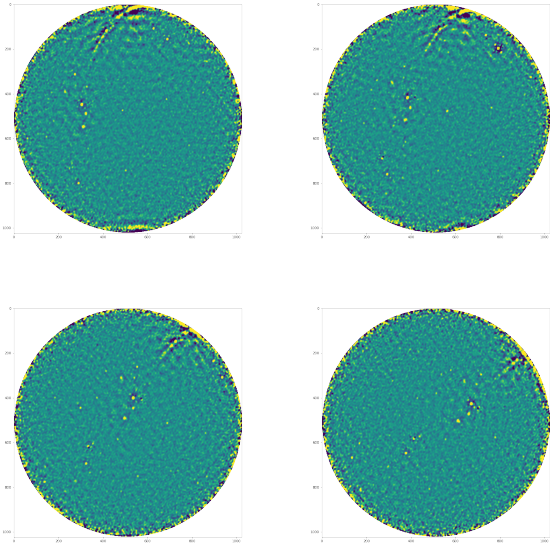


Figure A.10: Clean AARTFAAC6 images.

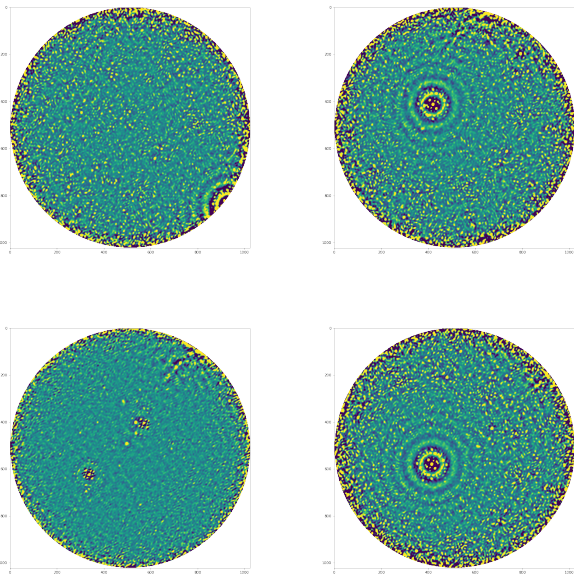


Figure A.11: RFI corruptions detected using the proposed method. Note that these occurred only 1 sub-band adjacently to the clean counterpart presented in the previous figure.

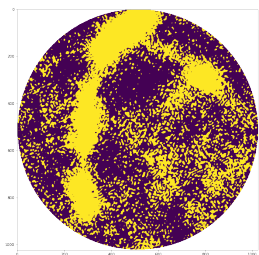


Figure A.12: Example of resulting image of correlation and imaging pipeline error.

Appendix B. Skymap Simulation Examples

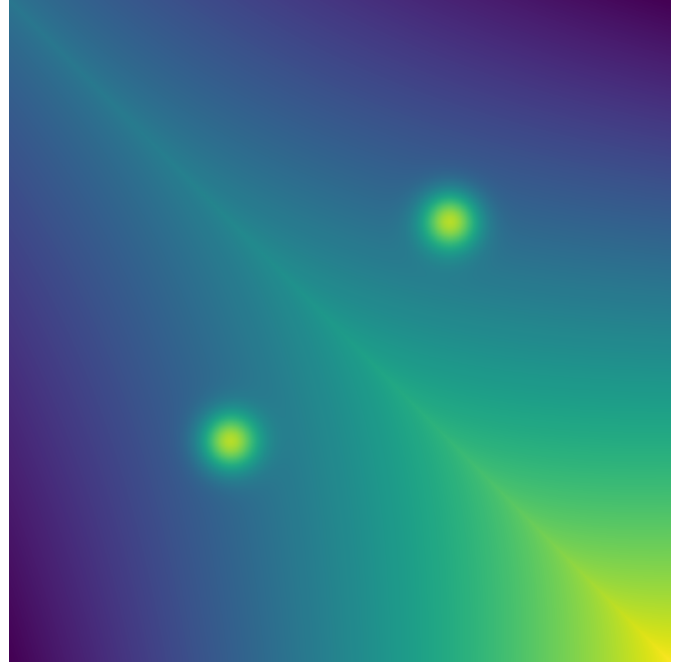


Figure B.13: The inhomogeneous galactic foreground & remnants map used in this work.

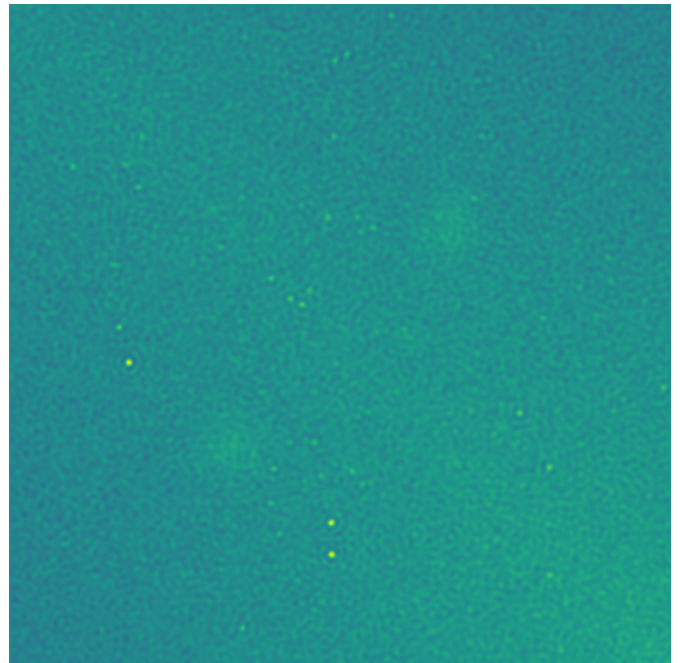


Figure B.14: Example of simulated single-channel source map used in our source detection experiments.

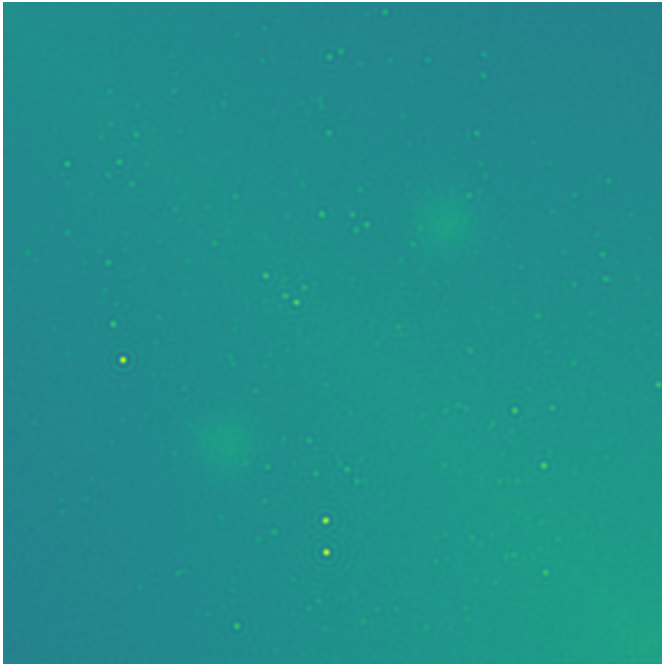


Figure B.15: Example of simulated integrated source map used in our source detection experiments.

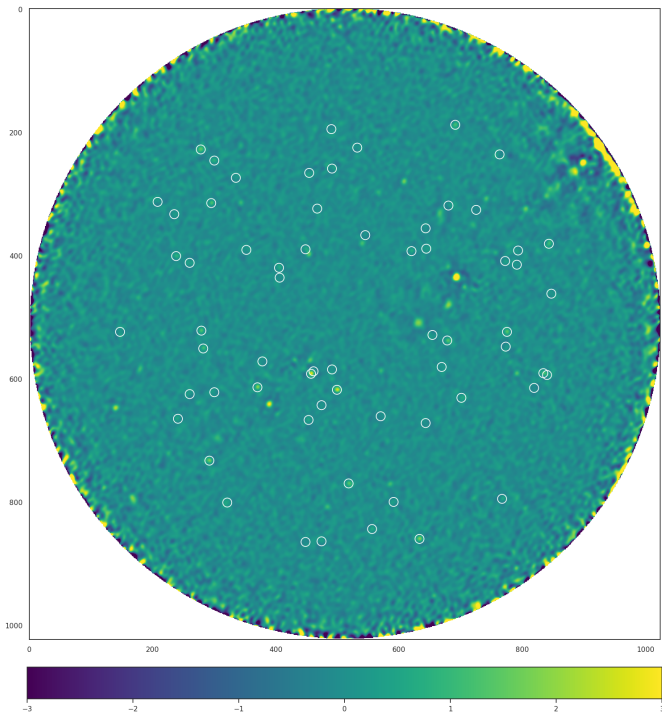


Figure B.16: Example of simulated source map used in our source detection experiments. Locations of simulated sources are indicated.

Appendix C. Sigma-clip Iterations

We noted that since we have continuous estimates of the local statistics using convolutions, we do not require many iterations to do peak detection. This can be seen in Figure C.17, where the performance of the source-finder is plotted as a function of

the sigma-clip iteration. It is shown that after the first step, we already retrieve many more false positives than true positives.

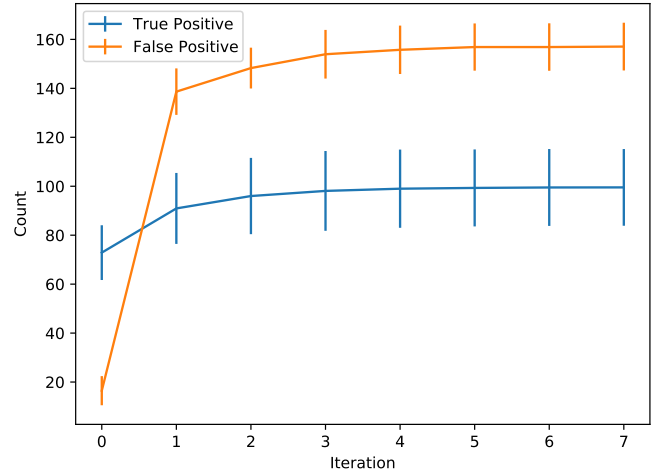


Figure C.17

Appendix D. Additional Dispersed Bursts from Real Data

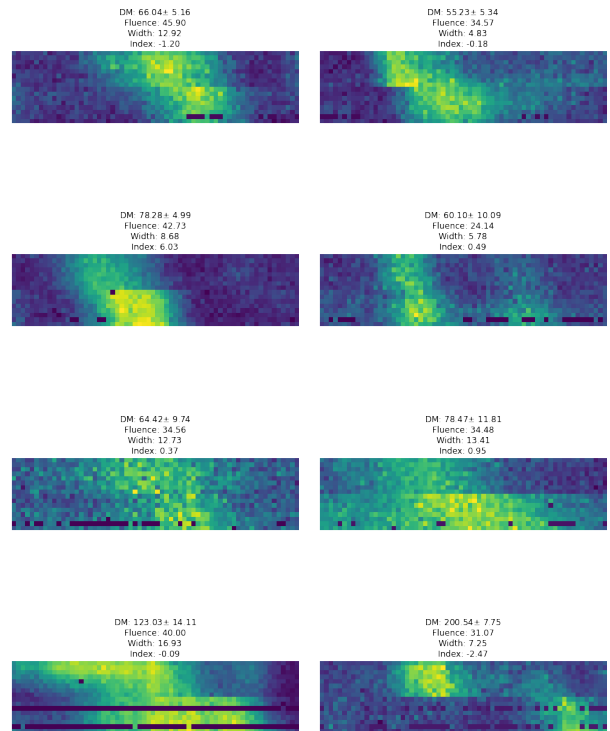


Figure D.18: Transient candidates from a 5-hour survey on 2019-09-01 18:55.

Appendix E. Statistical Analysis of Source-finding

In the following, we perform a statistical analysis on how detecting sources in separate sub-bands individually improves our type 2 error rates. We compare against averaging (with

independent noise and constant signal) after applying perfect de-dispersion. First and foremost, this is unattainable in practice: one would have to apply source-detection in images de-dispersed against all possible DM. This is computationally intractable. Secondly, the assumptions required are not realistic in practice. Alternatively, performing detection in the sub-bands individually still gives us a type 2 error improvement rate while being computationally feasible.

Appendix E.1. Single Subband

Consider a signal observed in a single passband. It is corrupted with Gaussian noise:

$$X = S + E \quad (\text{E.1})$$

with $E \sim \mathcal{N}(0, \sigma^2)$. We set a threshold that defines our type 1 error rate (i.e., false positives) at $\kappa\sigma$. Under type 1 error, we consider $S = 0$. That is, what is the probability that we conclude a detection when there is actually only noise. The standardised score is $Z = \frac{X}{\sigma}$. The probability of such a type 1 error is

$$\begin{aligned} \Pr(Z > \kappa) &= 1 - \Pr(Z \leq \kappa) \\ &= 1 - \Pr(X \leq \kappa\sigma) \\ &= 1 - \Phi(\kappa\sigma) \end{aligned} \quad (\text{E.2})$$

Next, we consider the type 2 error rate. This expresses the probability that we neglect actual sources ($S > 0$), i.e., false negatives. We have

$$\begin{aligned} \Pr(X \leq \kappa\sigma \mid S) &= \Pr\left(X \leq \frac{\kappa\sigma - S}{\sigma}\right) \\ &= \Phi\left(\kappa - \frac{S}{\sigma}\right), \end{aligned} \quad (\text{E.3})$$

and so our defined κ and the signal-to-noise ratio of the source define our probability of neglecting it.

Appendix E.2. Perfect dedispersion

Consider a signal that we observe in multiple passbands. We average it after correcting perfectly for the delay. Assuming perfect independent Gaussianity with equal variances and equal signals in all channels, our signal to noise ratio improves with a factor N .

$$\bar{X} = \frac{1}{n} \sum_{i=1}^n [S + E_i] = S + \bar{E} \quad (\text{E.4})$$

$$\begin{aligned} \text{SNR} &:= \frac{S^2}{\mathbb{E}[\bar{E}^2]} \\ &= \frac{S^2}{\text{Var}[\bar{E}]} \\ &= \frac{S^2}{\frac{1}{n}\sigma^2} \end{aligned} \quad (\text{E.5})$$

and so the noise level decreases by \sqrt{n} .

Since we keep the false negative rate fixed, defined by $\kappa\sigma$, our type 2 error improves. For $S > 0$ we have

$$\Pr(\bar{X} \leq \kappa\sigma \mid S) = \Phi\left(\kappa - \sqrt{n}\frac{S}{\sigma}\right). \quad (\text{E.6})$$

With $n > 1$ this is an improvement over the single-band case.

Appendix E.3. Wrong dedispersion

Often, subbands are averaged in order to improve signal-to-noise ratios. However, in the face of a dispersed signal, doing so can actually wash out the signal. In the extreme case, we only observe it in a single band. Integrating that out would be equal to considering

$$\hat{X} = \frac{1}{N} \left[S + \sum_{i=1}^N E_i \right] \quad (\text{E.7})$$

which is equal to reducing the signal with \sqrt{n} .

$$\text{SNR} := \frac{\frac{1}{n^2}S^2}{\frac{1}{n}\sigma^2} \quad (\text{E.8})$$

Considering the same type 1 error $\kappa\sigma$ then increases our type 2 error:

$$\Pr(\hat{X} \leq \kappa\sigma \mid S) = \Phi\left(\kappa - \frac{S}{\sqrt{n}\sigma}\right) \quad (\text{E.9})$$

Appendix E.4. No dedispersion & independent detection.

By doing detection in multiple subbands simultaneously, we are effectively “throwing the dice” n times. By doing so, we obtain an increased type 1 error. The probability of obtaining a false positive simply increases if you consider more trials. Thus, to make a fair comparison with the other methods we should adjust for this.

The probability of a type 1 error in this case is (for $S = 0$):

$$\begin{aligned} \Pr(Z_1 > k \vee \dots \vee Z_n > k) &= 1 - \Pr(Z_1 \leq k \wedge \dots \wedge Z_n \leq k) \\ &= 1 - \prod_{i=1}^n \Pr(Z_i \leq k) \\ &= 1 - \Pr(X \leq k\sigma)^n \\ &= 1 - \Phi(k\sigma)^n \end{aligned} \quad (\text{E.10})$$

Equating this with the type 1 error derived in [Equation E.2](#)

$$\begin{aligned} 1 - \Phi(k\sigma)^n &= 1 - \Phi(\kappa\sigma) \\ \iff \Phi(k\sigma) &= \Phi(\kappa\sigma)^{1/n} \\ \iff k\sigma &= \Phi^{-1}(\Phi(\kappa\sigma)^{1/n}) \end{aligned} \quad (\text{E.11})$$

Then, the type 2 error ($S > 0$) probability is:

$$\begin{aligned} \Pr(X_1 \leq k\sigma \wedge \dots \wedge X_n \leq k\sigma) &= \prod_{i=1}^n \Pr\left(X_i \leq \frac{k\sigma - S}{\sigma}\right) \\ &= \Phi\left(k - \frac{S}{\sigma}\right)^n \end{aligned} \quad (\text{E.12})$$

which clearly improves as n increases.

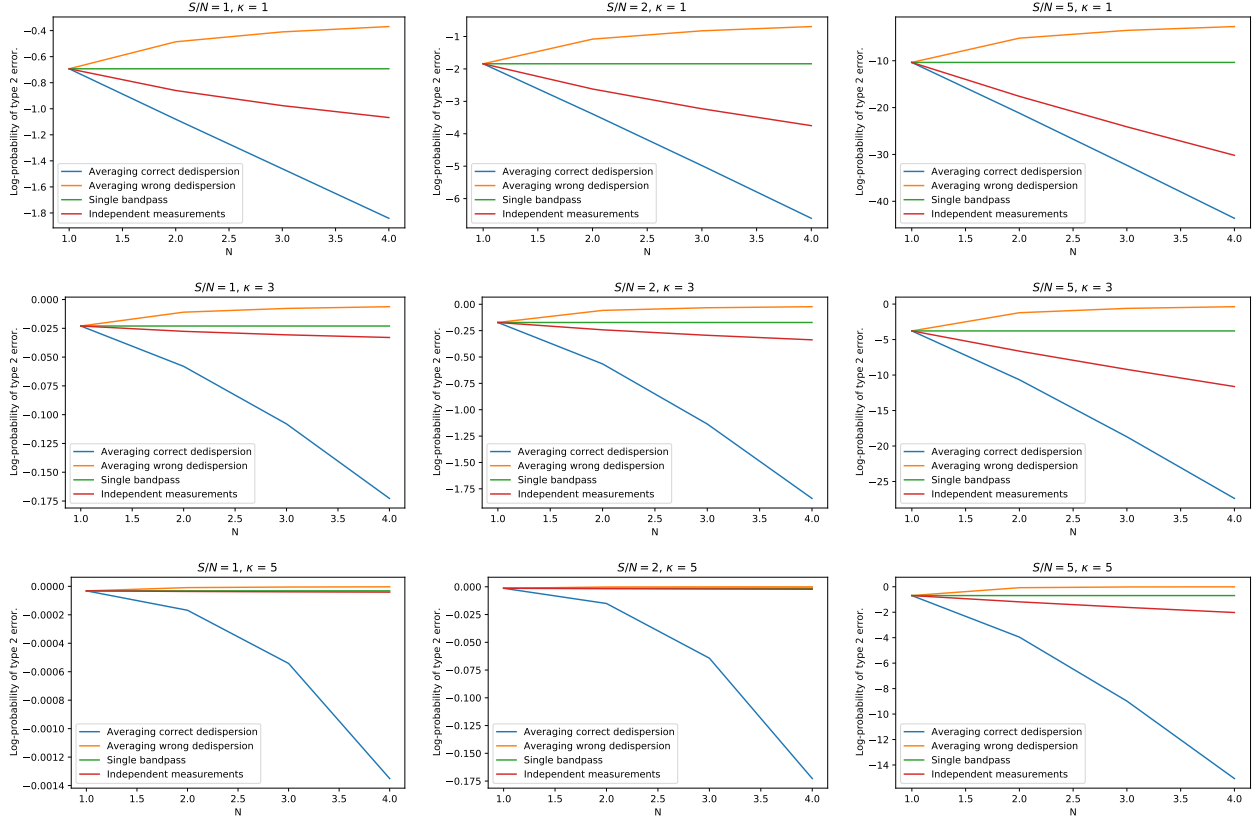


Figure E.19: Results for the statistical comparison of using multi-frequency source detection methods.

Appendix E.5. Comparison

Analytically relating these quantities is not trivial due to the CDFs. Instead, we switch to an empirical study by comparing the type 2 probabilities for different κ , n and S , fixing σ at unity. The results are shown in Figure E.19. Averaging clearly wins, but the assumptions required are rather strong.

1. Perfect dedispersion
2. Uncorrelated noise
3. Stable signal across all bands

If assumptions 1) and 2) are violated, we may actually risk amplifying the noise and end up in the case where we reduce the signal-to-noise ratio. Moreover, assumption 1) is infeasible in practice, as we would have to perform source-finding in images averaged for all possible DM. However, by running detections in separate subbands we and still gain a type 2 performance increase over not using the multiple bandpasses or wrong dedispersion, which is also frequently done.

Additionally, if running with high type 1 probability error is not a problem (which is the case for our proposed pipeline, as the neural network is effectively filtering out the false positives), then averaging is relatively less effective (see the $\kappa = 1$ and $\kappa = 3$ cases).

Finally, by correcting for dispersion by doing a DM sweep, the probability of a type 1 error increases, which we did not account for in this analysis.